Forced vibrations of a turbine blade undergoing regularized unilateral contact conditions through the wavelet balance method

Simon Jones, Mathias Legrand

Forced vibrations of a turbine blade undergoing regularized unilateral contact conditions through the wavelet balance method

Simon Jones[a], Mathias Legrand[b]

[a]*Department of Mechanical Engineering, Rose-Hulman Institute of Technology, Terre Haute, Indiana, USA 47803*
[b]*Department of Mechanical Engineering, McGill University, Montréal, Québec, Canada H3A 0C3*

SUMMARY

The method of weighted residuals can efficiently enforce time-periodic solutions of flexible structures experiencing unilateral contact. The Harmonic Balance Method (HBM) based on Fourier expansion of the sought solution is a common formulation, though wavelet bases that can sparsely define nonsmooth solutions may be superior. This hypothesis is investigated using a full three-dimensional blade with unilateral contact conditions on a set of N_c discrete contact points located at its tip. The unilateral contact conditions are first regularized and a distributional formulation in time is introduced allowing $L^2(\mathbb{S}^1)^N$ trial functions to properly approximate in the time-domain the solution to the governing equations. The mixed wavelet Petrov-Galerkin solutions are found to yield consistent or better results than HBM, with higher convergence rates and seemingly more accurate contact force prediction.

KEY WORDS: wavelet analysis, Petrov-Galerkin method, weak formulation, unilateral contact conditions, nonsmooth dynamics

1. INTRODUCTION

Efficiently predicting the vibratory responses of flexible structures which experience unilateral contact is becoming of high engineering importance primarily because of possible subsequent mechanical failure originated by fatigue. This type of response is increasingly common in industrial applications due to implementation of light materials and thin designs involving larger displacements together with tighter operating clearances between components. For example, consider aircraft engines where slender, twisted blades rotate at high rotational velocity within stationary casings where minimal clearance is desirable for turbine energy efficiency. Simulating contact between the blades and casing is not a trivial exercise since unilateral contact is usually described by inequalities and complementary conditions [49]. In the time domain, structural displacements and velocities which satisfy these non-penetration Signorini conditions are known to respectively feature absolute continuity and bounded variation only [41]. This implies displacements are not necessarily differentiable everywhere in the defined domain and velocities may exhibit jumps; these types of problems are generally referred to as *nonsmooth*. Broadly speaking, existence of solutions is still an open problem and intense research is devoted to the derivation of efficient time-stepping solution methods [1, 28].

This class of unilateral problems can also be approached using periodic vibration theory. This allows the original initial-value formulations to be transformed into formulations that are periodic in time [25]. In structural mechanics, two families of numerical techniques can efficiently describe approximated periodic solutions while maintaining computational efficiency. The first is commonly known as the *shooting method* which consists of finding the initial conditions that realize a periodic motion; for free responses, the period of the motion can also be an unknown. The overall approach relies on time integration of the governing equations over one period using a nonlinear solver which iterates on the initial conditions, and possibly the period. The second technique is based on *weighted residual formulations* which are of interest in the current investigation. This method involves approximating the solution using a set of time-dependent basis functions, called trial functions, and enforcing the respective residual error to be orthogonal to an independent set of weighting functions [24, 39]. The orthogonality is enforced using an inner product in the sense of a scalar product adequately defined on a functional Hilbert space. Unlike the shooting method which can become numerically sensitive to possible jumps in the velocity field, weighted residual techniques directly enforce the periodicity conditions while the remaining possibly regularized unilateral contact constraints and governing local equations of motion are satisfied in a weak integral sense [47]. It

is worth noting that the well-known Harmonic Balance Method (HBM) is a weighted residual approach where both the trial and weighting functions are Fourier series. The main goal of the current work is to explore relevant basis functions whose order of smoothness can be adapted to a particular system to attain accurate approximations and rapid convergence.

The paper is broken into five sections: Section 2 introduces the system of interest; Section 3 reviews the weighted residual formulation in time; Section 4 provides an overview of the different basis functions under investigation; Section 5 specifies the unilateral contact model; and Section 6 presents and compares results for a number of basis function combinations.

2. SYSTEM OF INTEREST

The current investigation is motivated by the contact interaction between blade tips and the surrounding casing in modern turbine engines. Structural contact is a consequence of improved energy efficient technology resulting in tight operating clearances between the rotor and casing; slight out-of-roundness of the casing can potentially yield severe damage [35, 36].

The model is simplified to a single blade, shown in Fig. 1; details of the model can be found in Section 5. The blade is subjected to unilateral contact by a rigid wall harmonically moving; the harmonic displacement is described by a time-dependent T-periodic function $y(t)$ which simulates the blade rotating within an out-of-round casing. Accordingly, the domain $\bar{\Omega} = \Omega \cup \Gamma_\mathrm{d} \cup \Gamma_\sigma \cup \Gamma_\mathrm{c}$ is occupied by the blade of interest where Ω is an open set of $\mathbb{R}^3$ whose boundary Γ is the union of non-intersecting sets: Γ_d, where the boundary displacement is prescribed; Γ_σ, where the boundary forces are prescribed; Γ_c, where the contact conditions are enforced.

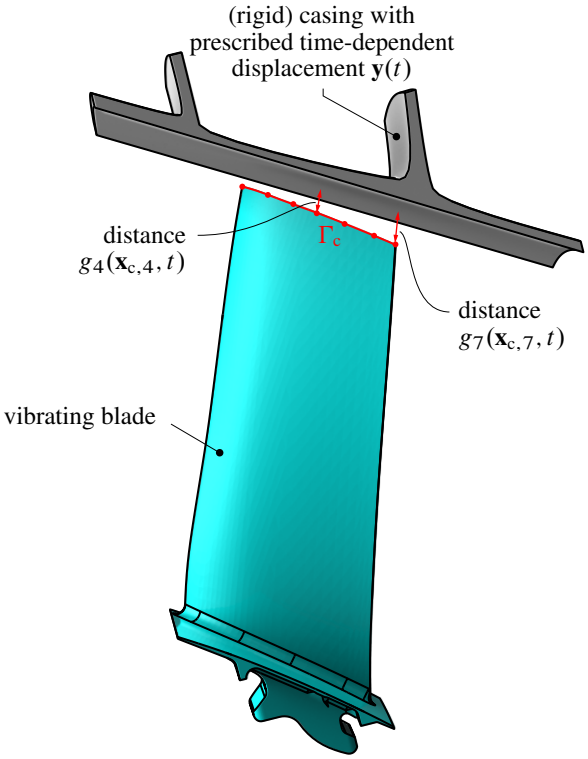

Figure 1. Schematic of the rotor blade undergoing unilateral contact conditions. The continuous contact interface Γ_c is approximated by $N_\mathrm{c} = 7$ contact points.

As a first approach, the contact interface Γ_c is simplified to $N_\mathrm{c} = 7$ contact points denoted $\mathbf{x}_{\mathrm{c},i} \in \mathbb{R}^3$, $i = 1, \ldots N_\mathrm{c}$ and located on the tip of the blade, see Fig. 2: they are used to enforce unilateral contact conditions in a pointwise fashion where friction is ignored (*i.e.* contact is purely in the radial direction). This pointwise contact approximates the pressure distribution over the blade tip; this is deemed an acceptable simplification given the other approximations made in the current investigation.

The *discrete* gap which exists between the tip and the oscillating casing boundary is uniquely defined by N_c gap functions as $g_i(\mathbf{x}_{c,i}, t) = g_{0,i} - \mathbf{n} \cdot (\mathbf{u}(\mathbf{x}_{c,i}, t) - \mathbf{y}(t))$, $i = 1, \ldots, N_c$ where $\mathbf{n}$ is the normal to the surface at the considered contact point, and $\mathbf{g}_0 = (g_{0,i})_{i=1,\ldots,N_c}$, the initial gap distances. These gap distances are stored in a vector $\mathbf{g}(\mathbf{x}_c, t) = (g_i(\mathbf{x}_{c,i}, t))_{i=1,\ldots,N_c}$. When the gap closes to 0, the blade tip comes into contact with the boundary and unilateral contact conditions must be satisfied. The existence of periodic solutions of period T is assumed. The unknown displacement $\mathbf{u}(\mathbf{x}, t)$ has to satisfy the following complementary boundary value problem:

1. local equation of motion

$$\rho \ddot{\mathbf{u}}(\mathbf{x}, t) - \mathbf{div}\, \overline{\overline{\boldsymbol{\sigma}}} = \mathbf{f}(\mathbf{x}, t), \quad \forall \mathbf{x} \in \Omega, \quad \forall t \tag{1}$$

2. linear strain and linear elasticity constitutive law

$$\overline{\overline{\boldsymbol{\varepsilon}}} = \frac{1}{2}\left(\overline{\overline{\nabla}}\mathbf{u} + \overline{\overline{\nabla}}^{\top}\mathbf{u}\right) \quad ; \quad \overline{\overline{\boldsymbol{\sigma}}} = \overline{\overline{\overline{\overline{\mathbf{D}}}}} : \overline{\overline{\boldsymbol{\varepsilon}}}, \quad \forall \mathbf{x} \in \bar{\Omega}, \quad \forall t \tag{2}$$

3. conditions of periodicity in time

$$\mathbf{u}(\mathbf{x}, t + T) = \mathbf{u}(\mathbf{x}, t) \quad \text{and} \quad \dot{\mathbf{u}}(\mathbf{x}, t + T) = \dot{\mathbf{u}}(\mathbf{x}, t), \quad \forall \mathbf{x} \in \bar{\Omega}, \quad \forall t \tag{3}$$

4. boundary condition in displacement

$$\mathbf{u}(\mathbf{x}, t) = \mathbf{0}, \quad \forall \mathbf{x} \in \Gamma_d, \quad \forall t \tag{4}$$

5. boundary condition in force

$$\overline{\overline{\boldsymbol{\sigma}}} \cdot \mathbf{n} = \mathbf{0}, \quad \forall \mathbf{x} \in \Gamma_\sigma, \quad \forall t \tag{5}$$

6. unilateral contact conditions (to be satisfied for each contact point)

$$g_i(\mathbf{x}_{c,i}, t) \geq 0 \quad ; \quad \lambda_i(t) \geq 0 \quad ; \quad \lambda_i(t) g_i(\mathbf{x}_{c,i}, t) = 0, \quad i = 1, \ldots, N_c, \quad \forall t \tag{6}$$

In the above equations, ρ signifies density, $\mathbf{f}(\mathbf{x}, t)$ the potential external body forces acting on the blade, the superscript $^{\top}$ denotes a transpose, and the dot superscript represents a temporal derivative. Structural damping is incorporated later by assuming β-damping of the elastic modulus, as detailed in Section 3. It is assumed in Eq. (5) that the potential other external loadings on Γ_σ (*e.g.* aerodynamic or pressure) are negligible compared to the unilateral contact loads.

The quantity $\boldsymbol{\lambda}(t) = (\lambda_i(t))_{i=1,\ldots,N_c}$, that mechanically is a contact force for node-wise contact conditions, stems from the enforced non-penetration conditions $\mathbf{g}(\mathbf{x}_c, t) \geq \mathbf{0}$ (to be read component-wise) and is necessarily non-negative (by convention). The complementarity condition $\lambda_i(t) g_i(\mathbf{x}_{c,i}, t) = 0$, $i = 1, \ldots, N_c$ states that the contact forces $\boldsymbol{\lambda}(t)$ and the corresponding distances $\mathbf{g}(\mathbf{x}_c, t)$ separating the blade tip contact points from the oscillating boundary may not be zero at the same time. These three conditions are such that the mathematical object pairing the contact force to the displacement is not a function in the usual sense. It is also known that the displacement field may be non-differentiable at given instants within the period of motion and the velocity field may be discontinuous. This motivates the derivation of numerical techniques capable of efficiently handling this nonsmoothness. As a first approach, the unilateral contact inequalities (6) are simplified and replaced by a penalty function; an exponential spring K_p is used to approximate the contact forces. For a single contact location, the gap $g_i(t)$ in Fig. 1 separates the tip of the blade and the exponential spring. The penalty function is of the form

$$f_{c,i}(\mathbf{u}(\mathbf{x}_{c,i}, t)) = \max\left(a_c(\mathrm{e}^{-\alpha g_i(\mathbf{x}_{c,i}, t)} - 1), 0\right). \tag{7}$$

Specific values for the penalty function are provided with the other model parameters in Section 5.

3. WEIGHTED RESIDUAL FORMULATIONS IN TIME

The method of weighted residuals is a classic method of obtaining numerical solutions to boundary value problems by expanding the sought solution as a finite sequence of time-dependent basis functions in a proper functional space [24], commonly referred to as *trial functions*. The periodicity conditions result in a problem which can be formulated on a circle in time denoted $\mathbb{S}^1$ where the period of the steady-state solution T has been normalized to 1 [4]. Accordingly, these basis functions are taken from the $L^2(\mathbb{S}^1)^N$ Hilbert space [21]. The subsequent residual is rendered orthogonal to a set a linearly independent functions of the same space, referred to as *weighting functions*, through an inner product. Trial and weighting functions may contain the same basis function but not necessarily: the Galerkin method is a special case where the weighting functions are taken from the same functional space as that of the trial functions; the Petrov-Galerkin method involves the selection of weighting function comprising a basis which is independent of the trial function [16]. The purpose of this study is to seek various Hilbert spaces of square integrable functions defined on the circle $\mathbb{S}^1$ which efficiently predict the displacement of the blade.

To solve Eqs. (1) through (6), the unknown displacement is expanded into a truncated series of N functions separated in space and time:

$$\mathbf{u}(\mathbf{x},t) = \sum_{i=1}^{N_{\text{nod}}} \boldsymbol{\vartheta}_i(\mathbf{x})\tilde{\mathbf{u}}_i(t) \tag{8}$$

where $\tilde{\mathbf{u}}_i(t)$ are the nodal displacements at the N_{nod} nodes of the mesh shown in Fig. 2, and $\boldsymbol{\vartheta}_i(\mathbf{x})$, the shape functions in space within the standard Finite Element Method which is here implemented for the spatial variable using quadratic hexahedral elements [3, 30]. The corresponding dynamics is then reduced

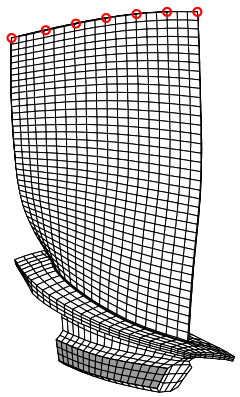

Figure 2. Finite element mesh of rotor blade; red dot shows unilateral contact nodes

through a slightly adapted version of the Craig-Bampton method [2, 26]. The blade itself is a considered as the unique substructure of the system, its root defining Γ_{d} is clamped and the N_{c} nodal displacements in the radial direction at the contact points (red nodes in Fig. 2) form the *boundary degrees-of-freedom*. The remaining *internal degrees-of-freedom* are synthesized. The resulting truncated set of *component modes* and full set of *static modes*, which capture the dynamics of the contact interface in our study, are then calculated. This yields the following reduced-order vector ordinary differential equation of size N in the Craig-Bampton basis:

$$\mathbf{M}\ddot{\tilde{\mathbf{u}}}(t) + \mathbf{C}\dot{\tilde{\mathbf{u}}}(t) + \mathbf{K}\tilde{\mathbf{u}}(t) = \mathbf{f}_{\text{ext}}(\tilde{\mathbf{u}}(t),t) \tag{9}$$

where $N \ll N_{\text{nod}}$, together with the remaining periodicity conditions in time and the unilateral contact conditions. Here $\mathbf{M}$ and $\mathbf{K}$ are the base-constrained mass and stiffness matrices for the blade, and β-damping is enforced such that $\mathbf{C} = \beta\mathbf{K}$ to account for structural damping. The displacement vector $\tilde{\mathbf{u}}(t)$ in Eq. (9) stores the temporal unknowns $\tilde{u_i}(t)$, $i = 1,\ldots,N$. Similarly, $\mathbf{f}_{\text{ext}}(\tilde{\mathbf{u}}(t),t)$ stores the reduced external forcing functions, if any, as well as the reduced contact forces stemming from the regularized contact force introduced in Eq. (7).

The remainder of the derivation involves a weighted residual formulation in the *time* dimension. Three forms of the weighted residual method are discussed: the strong integral form, the weak form, and the distributional formulation. For this discussion, it is understood that $\tilde{\mathbf{u}}$ (the trial functions) and $\tilde{\mathbf{v}}$ (the weighting functions) are time-dependent vectors, *i.e.* $\tilde{\mathbf{u}}(t)$ and $\tilde{\mathbf{v}}(t)$, but for the sake of clarity the (t) is omitted below.

3.1. Strong integral form

The standard weighted residual formulation of a differential equation is commonly termed the strong form. Taking the inner product of Eq. (9) with a weighting function stored column-wise in $\mathbf{v}$ results in the strong integral form of the equation: find $\tilde{\mathbf{u}} \in H^2(\mathbb{S}^1)^N$ such that

$$\forall \tilde{\mathbf{v}} \in L^2(\mathbb{S}^1)^N, \quad \int_{\mathbb{S}^1} \left(\tilde{\mathbf{v}}^\top \mathbf{M} \ddot{\tilde{\mathbf{u}}} + \tilde{\mathbf{v}}^\top \mathbf{C} \dot{\tilde{\mathbf{u}}} + \tilde{\mathbf{v}}^\top \mathbf{K} \tilde{\mathbf{u}} - \tilde{\mathbf{v}}^\top \mathbf{f}_{\text{ext}}(\tilde{\mathbf{u}}, t) \right) \mathrm{d}t = 0 \tag{10}$$

This strong form of the equation is not necessarily the best framework for obtaining a solution [30]; for this example involving a vector ordinary differential equation of order 2, the solution must be at least H^2, limiting the permissible basis of trial functions*.

3.2. Weak form

The respective weak form of the weighted residual statement can be obtained by performing one integration by parts over the domain $\mathbb{S}^1$ for all terms containing a double time derivative in Eq. (10). This results in: find $\tilde{\mathbf{u}} \in H^1(\mathbb{S}^1)^N$ such that

$$\forall \tilde{\mathbf{v}} \in H^1(\mathbb{S}^1)^N, \quad \int_{\mathbb{S}^1} \left(-\dot{\tilde{\mathbf{v}}}^\top \mathbf{M} \dot{\tilde{\mathbf{u}}} + \tilde{\mathbf{v}}^\top \mathbf{C} \dot{\tilde{\mathbf{u}}} + \tilde{\mathbf{v}}^\top \mathbf{K} \tilde{\mathbf{u}} - \tilde{\mathbf{v}}^\top \mathbf{f}_{\text{ext}}(\tilde{\mathbf{u}}, t) \right) \mathrm{d}t = 0 \tag{11}$$

The integral form of the weak formulation offers the advantage of shifting a portion of the functional smoothness requirement from the trial functions onto the weighting functions. More precisely, both the trial and weighting functions must now be H^1. This allows the trial functions to be chosen from a wider permissible space [30].

3.3. Formulation in a distributional sense

The above procedure of obtaining the solution from the weak formulation by performing integration by parts on the weighted residual statement can be extended one step further. Theoretically, this extension is not necessary since it is known that displacements should be absolutely continuous in time, though it may assist in the numerical derivations and allow very simple basis functions to be considered [45]. A weaker formulation is proposed by integrating again the terms involving time derivatives of the trial functions. This formulation can be understood in the sense of distributions, also known as generalized functions, *ie*: find $\tilde{\mathbf{u}} \in L^2(\mathbb{S}^1)^N$ such that

$$\forall \tilde{\mathbf{v}} \in H^2(\mathbb{S}^1)^N, \quad \int_{\mathbb{S}^1} \left(\ddot{\tilde{\mathbf{v}}}^\top \mathbf{M} \tilde{\mathbf{u}} - \dot{\tilde{\mathbf{v}}}^\top \mathbf{C} \tilde{\mathbf{u}} + \tilde{\mathbf{v}}^\top \mathbf{K} \tilde{\mathbf{u}} - \tilde{\mathbf{v}}^\top \mathbf{f}_{\text{ext}}(\tilde{\mathbf{u}}, t) \right) \mathrm{d}t = 0 \tag{12}$$

Here the double time differential on the field variable is transferred to the weighting function and the continuity requirement on the trial function is reduced. As discussed later, the desired displacement functions $\tilde{\mathbf{u}}$ can now be described using a series of constant piecewise functions for instance.

3.4. Time discretization

Let each nodal displacement $\tilde{u_i}(t)$ be approximated by a combination of M linearly independent trial functions $q_k(t)$, $k = 1, \ldots, M$ defined on $t \in \mathbb{S}^1$. Similarly, let each $\tilde{v_i}(t)$ be approximated by a combination of linearly independent weighting functions $p_k(t)$, $k = 1, \ldots, M$ also defined on $t \in \mathbb{S}^1$.

*A very brief description of the Sobolev spaces used herein can be found in the Appendix.

Collectively, this leads to

$$\tilde{u_i}(t) = \sum_{k=1}^{M} a_{ik} q_k(t) \quad \text{and} \quad \tilde{v_i}(t) = \sum_{k=1}^{M} b_{ik} p_k(t), \quad i = 1, \ldots, N \tag{13}$$

or, equivalently in a vector form:

$$\tilde{\mathbf{u}}(t) = \boldsymbol{\Theta}(t)\mathbf{a} \quad \text{and} \quad \tilde{\mathbf{v}}(t) = \boldsymbol{\Gamma}(t)\mathbf{b} \tag{14}$$

In Eq. (14), $\boldsymbol{\Theta}(t)$ and $\boldsymbol{\Gamma}(t)$ are rectangular matrices of dimension $N \times NM$; $\mathbf{a}$ and $\mathbf{b}$ are vectors of size $NM \times 1$.

Each of the strong, weak, and distributional formulations can now be discretized with proper time-dependent basis functions. The overall goal of this paper is to discuss the numerical properties of certain wavelet bases to efficiently solve the problem of interest. Depending on the selected formulation, the order of derivation acting on $\tilde{\mathbf{u}}(t)$ and $\tilde{\mathbf{v}}(t)$ (*i.e.* $\boldsymbol{\Theta}(t)$ and $\boldsymbol{\Gamma}(t)$ respectively) will affect the admissible basis functions. The arbitrariness of the weighing function in Eq. (10), (11), and (12) is reflected by the arbitrariness of vector $\mathbf{b}$ and the corresponding discretized versions are:

- strong integral form:

$$\int_{\mathbb{S}^1} \Big(\big(\boldsymbol{\Gamma}^\top \mathbf{M} \ddot{\boldsymbol{\Theta}} + \boldsymbol{\Gamma}^\top \mathbf{C} \dot{\boldsymbol{\Theta}} + \boldsymbol{\Gamma}^\top \mathbf{K} \boldsymbol{\Theta} \big) \mathbf{a} - \boldsymbol{\Gamma}^\top \mathbf{f}_{\text{ext}}(\boldsymbol{\Theta}\mathbf{a}, t) \Big) \, \mathrm{d}t = 0 \tag{15}$$

- weak form:

$$\int_{\mathbb{S}^1} \Big(\big(-\dot{\boldsymbol{\Gamma}}^\top \mathbf{M} \dot{\boldsymbol{\Theta}} + \boldsymbol{\Gamma}^\top \mathbf{C} \dot{\boldsymbol{\Theta}} + \boldsymbol{\Gamma}^\top \mathbf{K} \boldsymbol{\Theta} \big) \mathbf{a} - \boldsymbol{\Gamma}^\top \mathbf{f}_{\text{ext}}(\boldsymbol{\Theta}\mathbf{a}, t) \Big) \, \mathrm{d}t = 0 \tag{16}$$

- distributional form:

$$\int_{\mathbb{S}^1} \Big(\big(\ddot{\boldsymbol{\Gamma}}^\top \mathbf{M} \boldsymbol{\Theta} - \dot{\boldsymbol{\Gamma}}^\top \mathbf{C} \boldsymbol{\Theta} + \boldsymbol{\Gamma}^\top \mathbf{K} \boldsymbol{\Theta} \big) \mathbf{a} - \boldsymbol{\Gamma}^\top \mathbf{f}_{\text{ext}}(\boldsymbol{\Theta}\mathbf{a}, t) \Big) \, \mathrm{d}t = 0 \tag{17}$$

The resulting nonlinear equations can generically be recast in the following form

$$\mathbf{G}\mathbf{a} - \mathbf{f}(\mathbf{a}) = \mathbf{0} \tag{18}$$

where $\mathbf{G}\mathbf{a}$ and $\mathbf{f}(\mathbf{a})$ respectively stand as the linear internal and the nonlinear external contributions in Eq. (15), (16), and (17).

3.5. Matrix condensation

It is useful to note that after discretization in space and time, the penalty-like contact force is applied to only seven degree-of-freedoms (*i.e.* the radial components of the contact nodes). This allows the equations of motion to be condensed to seven active degrees-of-freedom. Consider the partitioning of Eq. (18) into passive p and active a degrees-of-freedom as follows [13]:

$$\begin{bmatrix} \mathbf{G}_{\text{pp}} & \mathbf{G}_{\text{pa}} \\ \mathbf{G}_{\text{ap}} & \mathbf{G}_{\text{aa}} \end{bmatrix} \begin{pmatrix} \mathbf{a}_{\text{p}} \\ \mathbf{a}_{\text{a}} \end{pmatrix} - \begin{pmatrix} \mathbf{0} \\ \mathbf{f}_{\text{a}}(\mathbf{a}_{\text{a}}) \end{pmatrix} = \begin{pmatrix} \mathbf{0} \\ \mathbf{0} \end{pmatrix}. \tag{19}$$

In this form $\mathbf{f}_{\text{a}}(\mathbf{a}_{\text{a}})$ is the displacement-dependent nonlinear contact force. The first block row of Eq. (19) is linear and gives

$$\mathbf{a}_{\text{p}} = -\mathbf{G}_{\text{pp}}^{-1} \mathbf{G}_{\text{pa}} \mathbf{a}_{\text{a}} \tag{20}$$

resulting in the condensation equation

$$\big(\mathbf{G}_{\text{aa}} - \mathbf{G}_{\text{ap}} \mathbf{G}_{\text{pp}}^{-1} \mathbf{G}_{\text{pa}} \big) \mathbf{a}_{\text{a}} - \mathbf{f}_{\text{a}}(\mathbf{a}_{\text{a}}) = \mathbf{0} \tag{21}$$

or

$$\bar{\mathbf{G}}\mathbf{a}_{\mathrm{a}} - \bar{\mathbf{f}}(\mathbf{a}_{\mathrm{a}}) = \mathbf{0} \tag{22}$$

for simplicity. The square matrix and vectors of Eq. (22) are of size $7M$. Eq. (22) is nonlinear and must be solved using an appropriate solver. Condensing the equations of motion reduces the number of unknowns in the nonlinear solution, hence reducing computational times and generally increasing the rate of convergence.

4. TRIAL AND WEIGHTING FUNCTION BASES

The selection of functional bases to be used in the above approaches is an important factor in approximation accuracy and computational efficiency [3, 30]. *A priori* selection of the optimal bases for unilateral contact problems is not a trivial matter due to potential nonsmoothness of the response. In the current investigation a number of bases are investigated to compare the quality of approximation, including Fourier functions, B-spline wavelets, Daubechies wavelets, and Haar wavelets.

4.1. Harmonic balance and Fourier series

The harmonic balance method (HBM) is a special case of the weighted residual method where the Fourier basis is used for both the trial and weighting functions [33]. This technique is particularly effective when dealing with smooth nonlinear systems; convergence is often reached with very few terms. It has been used to study steady state response of turbine engine blades with friction dampers using a multiterm approximation [46]. This approach was extended to unilateral contact and friction conditions [27] through an Alternating Frequency/Time domain strategy proposed by Cameron *et al.* [10] and Pilipchuk [38]. It is worthy to note that the HBM formulations of Eqs. (15), (16), and (17) are identical.

The Fourier basis for $L^2(\mathbb{S}^1)$ is defined as $\{1\} \cup \{\cos(2m\pi t), \sin(2m\pi t) | m \in \mathbb{N}^*\}$ where m signifies the harmonic number of the function. The first six functions are shown in Fig. 3.

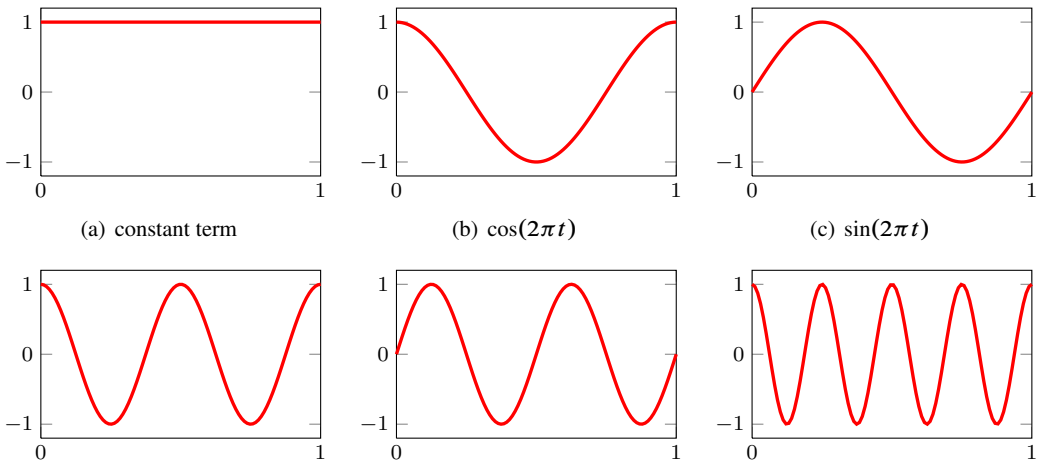

(a) constant term (b) $\cos(2\pi t)$ (c) $\sin(2\pi t)$

(d) $\cos(4\pi t)$ (e) $\sin(4\pi t)$ (f) $\cos(6\pi t)$

Figure 3. First six functions of the Fourier basis

Fourier basis functions feature an infinite degree of smoothness. While this property can be beneficial in some cases, it is unclear whether Fourier functions are optimal when simulating potentially nonsmooth problems. It is possible that a large number of harmonics would be required to accurately capture the nonsmooth response, or the approximation may exhibit Gibbs phenomenon at localized discontinuities in the sought displacement and velocity fields. Accordingly, other basis functions featuring a lesser degree of functional smoothness are explored.

4.2. Brief review of discrete orthogonal wavelets

Discrete orthogonal wavelet families are composed of highly localized, oscillatory functions which provide a basis of $L^2(\mathbb{R})$ and can be adapted to the periodic domain $L^2(\mathbb{S}^1)$ [31]. These localized characteristics, or compact support, allow sparse representation of piecewise signals including transients and singularities [9]. This makes them useful functions for use in the Galerkin approach when nonsmooth solutions are predicted [43]. There are a large number of wavelet families and definitions thereof; both Mallat [31] and Strang [43] provide excellent introductions to wavelet theory and history. Galerkin methods using appropriate discrete wavelet families as the trial functions have been shown to accurately approximate the solutions to both ordinary and partial differential equations [5, 6, 37, 48, 12, 8].

The discrete wavelet family is built from scaling functions $\phi(t)$ and wavelet functions $\psi(t)$. These functions are analogous to the low-pass and high-pass filters of a filter bank [43]; decomposition using scaling functions will give a "smoothed" approximation of the original signal, while decomposition using wavelet functions provides the details of the signal, or high-frequency content.

The exact decomposition of a continuous time signal $\tilde{u}_i(t)$ can be written

$$\tilde{u}_i(t) = \sum_k g_k \phi_{J,k}(t) + \sum_{j=J}^{m} \sum_{\ell} h_{j,\ell} \psi_{j,\ell}(t) \tag{23}$$

and

$$\phi_{J,k}(t) = 2^{J/2} \phi(2^J t - k) \tag{24}$$

$$\psi_{J,k}(t) = 2^{J/2} \psi(2^J t - k) \tag{25}$$

where $J, k \in \mathbb{Z}$; J is the dilation parameter (*i.e.* level), k is the translation parameter, and m is the maximum resolution given by the sampling rate of the function $\tilde{u}_i(t)$.

The span of the scaling functions at level J is commonly denoted $\mathbf{V}_J$, while the wavelet span is denoted $\mathbf{W}_J$. For orthogonal wavelet families, $\mathbf{W}_J$ is the orthogonal complement to $\mathbf{V}_J$ in $\mathbf{V}_{J+1}$

$$\mathbf{V}_{J+1} = \mathbf{V}_J \oplus \mathbf{W}_J. \tag{26}$$

Provided the wavelet family is orthogonal [43], the space of square-integrable functions on the real line $L^2(\mathbb{R})$ can be decomposed using multiresolution analysis as a nested sequence of closed subspaces [31]

$$\cdots \subset \mathbf{V}_{-2} \subset \mathbf{V}_{-1} \subset \mathbf{V}_0 \subset \mathbf{V}_1 \subset \mathbf{V}_2 \subset \cdots \subset L^2(\mathbb{R}) \tag{27}$$

such that

$$\lim_{J \to \infty} \mathbf{V}_J = L^2(\mathbb{R}). \tag{28}$$

This implies that $\mathbf{V}_J$, the subspace composed of the set of scaling functions at level J, can approximate any function in $L^2(\mathbb{R})$. A reduced orthonormal basis of $L^2(\mathbb{R})$ is constructed by truncating the wavelet terms, resulting in

$$\tilde{u}_i(t) = \sum_k u_k \phi_{J,k}(t) \tag{29}$$

The accuracy of this approximation increases as the level J is increased. This property of the scaling functions makes them excellent trial and weighting functions in weighted residual methods because they can be adapted to the accuracy level required. The reduced orthonormal basis of scaling functions is used in the current investigation. This approach of increasing the level of scaling functions, rather than including wavelet functions to increase approximation accuracy, is a common approach in the literature [34] and used in the bulk of the applicable references cited in this paper.

4.2.1. Periodization of wavelet families Standard wavelet definitions (*i.e.* scaling and wavelet functions) are commonly built on the real line. The functions can be adapted to periodic functions of $L^2(\mathbb{S}^1)$ by utilizing a standard periodization technique [31, 17, 32]. Let $\phi^{(p)}(t)$ be the periodized form of the scaling function $\phi(t)$ defined on $\mathbb{R}$

$$\phi_{J,k}^{(p)}(t) = \sum_{\ell \in \mathbb{Z}} \phi_{J,k}(t - \ell) \qquad 0 \leq k \leq 2^J - 1. \tag{30}$$

This is equivalent to "wrapping around" the support $\mathbb{R}$ on $\mathbb{S}^1$ through summation. The finite size of the interval results in the condition $J \geq 0$

$$\mathbf{V}_0 \subset \mathbf{V}_1 \subset \mathbf{V}_2 \subset \mathbf{V}_3 \subset \cdots \subset L^2(\mathbb{S}^1) \tag{31}$$

such that

$$\lim_{J \to \infty} \mathbf{V}_J = L^2(\mathbb{S}^1). \tag{32}$$

A number of periodic discrete wavelet families exist [31]. The investigation considers three families to determine how they perform in unilateral, nonsmooth contact problems: B-spline, Daubechies, and Haar.

4.3. Orthogonal cubic B-spline scaling functions

The scaling function ϕ for the orthogonal cubic B-spline wavelet family built on $\mathbb{R}$ is given as [7]

$$\phi(t) = \sum_k c_k B_3(t - k) \tag{33}$$

where cubic B-spline $B_3(t)$ can be written using the following formulas

$$B_3(t) = \begin{cases} t^3/6 & (0 \leq t \leq 1) \\ -t^3/2 + 2t^2 - 2t + 2/3 & (1 \leq t \leq 2) \\ t^3/2 - 4t^2 + 10t - 22/3 & (2 \leq t \leq 3) \\ -t^3/6 + 2t^2 - 8t + 32/3 & (3 \leq t \leq 4) \\ 0 & (\text{otherwise}). \end{cases} \tag{34}$$

The coefficients c_k can be determined using [7]

$$c_k = c_{-k} = \frac{1}{\pi} \int_0^\pi \frac{\cos(k\xi)}{\sqrt{p_3(\cos \xi)}} \, \mathrm{d}\xi \qquad (k \geq 0) \tag{35}$$

where k is an integer. The cubic polynomial p_3 is given as

$$p_3(\cos(\xi)) = \frac{1}{630}(\cos^3(\xi) + 60\cos^2(\xi) + 297\cos(\xi) + 272). \tag{36}$$

Numerical simulations showed that truncating the summation in Eq. (33) at $-50 \leq k \leq 50$ is sufficient; larger k terms add negligibly to the summation. After periodization to $\mathbb{S}^1$ and normalization by $\int_0^1 \phi_{J,k}(t) \, \mathrm{d}t = 1$ [11], sample orthogonal cubic B-spline scaling functions for $J = 0, 1, \ldots, 5$ are shown in Fig. 4

4.4. Daubechies Wavelets

The Daubechies wavelet family is defined by a set of L filter coefficients $\{p_\ell : \ell = 0, 1, \ldots, L - 1\}$, where L is an even integer. The scaling function is defined by the fundamental two-scale equation [11]

$$\phi(t) = \sum_{\ell=0}^{L-1} p_\ell \, \phi(2t - \ell) \tag{37}$$

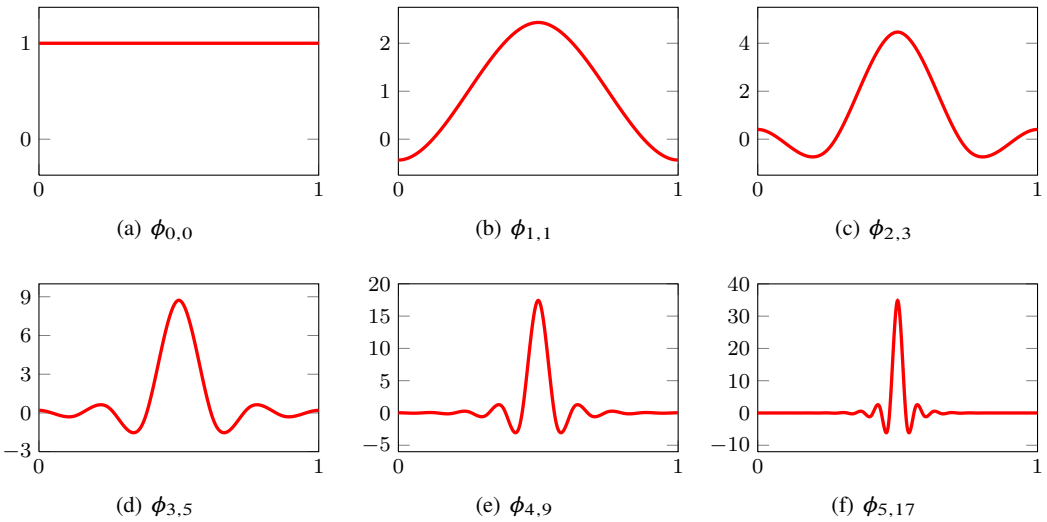

(a) $\phi_{0,0}$ (b) $\phi_{1,1}$ (c) $\phi_{2,3}$

(d) $\phi_{3,5}$ (e) $\phi_{4,9}$ (f) $\phi_{5,17}$

Figure 4. Examples of the first six levels of periodized orthogonal cubic B-spline scaling functions

which has fundamental support over the finite intervals $[0, L-1]$. This equation can be used to determine the value of the scaling function at dyadic points $t = n/2^J, n = 0, 1, \ldots$ using the algorithm provided by Chen *et al.* [11]. The exact solution for derivatives of the Daubechies scaling functions are also available up to derivative order $L/2 - 1$.

The wavelet filter coefficients p_ℓ were derived by Daubechies to produce scaling and wavelet functions with specific properties [11, 14], some of which include:

- the area under the scaling function is unity

$$\int_{-\infty}^{\infty} \phi(t)\,\mathrm{d}t = 1 \tag{38}$$

- the coefficients sum to two

$$\sum_{\ell=0}^{L-1} p_\ell = 2 \tag{39}$$

- the scaling function and its translates are orthogonal

$$\int_{-\infty}^{\infty} \phi(t)\phi(t-k)\,\mathrm{d}t = \delta_{0,k} \qquad k \in \mathbf{Z} \tag{40}$$

The corresponding scaling functions are highly nonsmooth and fractal in nature: as one increases the resolution of the functions, the shape does not converge but rather continues to increase in complexity. This makes accurately estimating the inner products of such scaling functions with each other prone to error when numerical integration is used [40].

When Daubechies scaling functions are used in a Galerkin approach, it is necessary to derive the inner products of the scaling function with itself or derivatives of itself. The exact solution to these inner products can be found by using the recursive nature of the fundamental equation on $L^2(\mathbb{R})$ [5, 11]; the solution to these inner products are commonly referred to as connection coefficients. When Daubechies scaling functions are periodized on $\mathbb{S}^1$, the wrapping procedure results in functions which are no longer scale-invariant at low J values (scale-invariance requires wavelets at any scale to be a pure dilation of the mother-wavelet). Fig. 5 provides examples of the periodized scaling functions for $L = 6$. Interestingly, the lack of scale-invariance for small J values does not invalidate the connection coefficient algorithms derived for unbounded domains; the connection coefficients can simply be wrapped around the periodic domain as necessary [40].

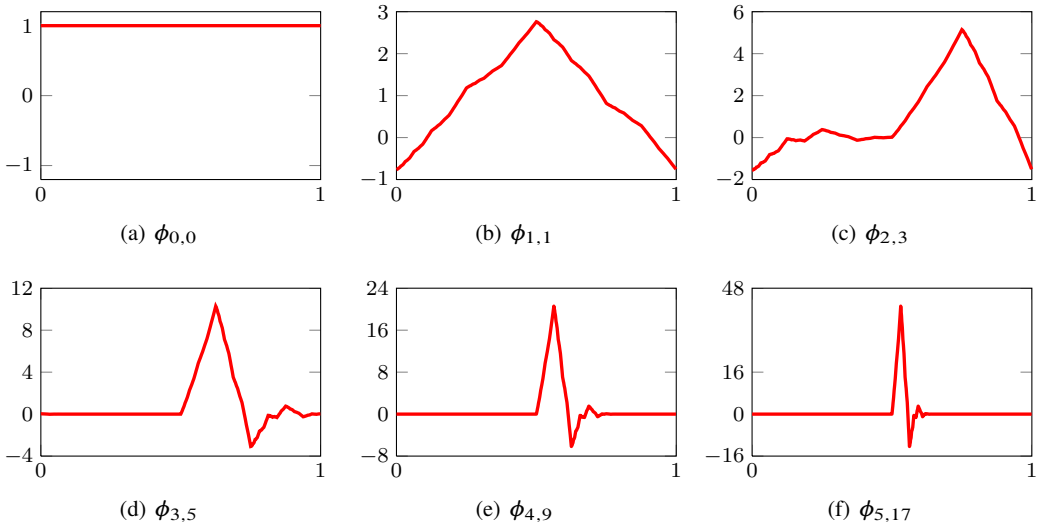

Figure 5. Examples of the first six levels of periodized 6 coefficient Daubechies scaling functions (DB6)

4.5. Haar scaling functions

The simplest Daubechies wavelet family requires only two filter coefficients ($p_0 = p_1 = 1$) and is commonly known as the Haar wavelet family [20]. The Haar scaling functions are rectangular tophat-type functions; the father scaling function is defined on $t \in \mathbb{R}$ as

$$\phi(t) = \begin{cases} 1 & (0 \leq t < 1) \\ 0 & (\text{otherwise}). \end{cases} \tag{41}$$

Since the compact support of the father scaling function is $\mathbb{S}^1$, the periodized function is equivalent. Example Haar scaling functions for $J = 0, 1, \ldots, 5$, normalized by Eq (38), are shown in Fig. 6.

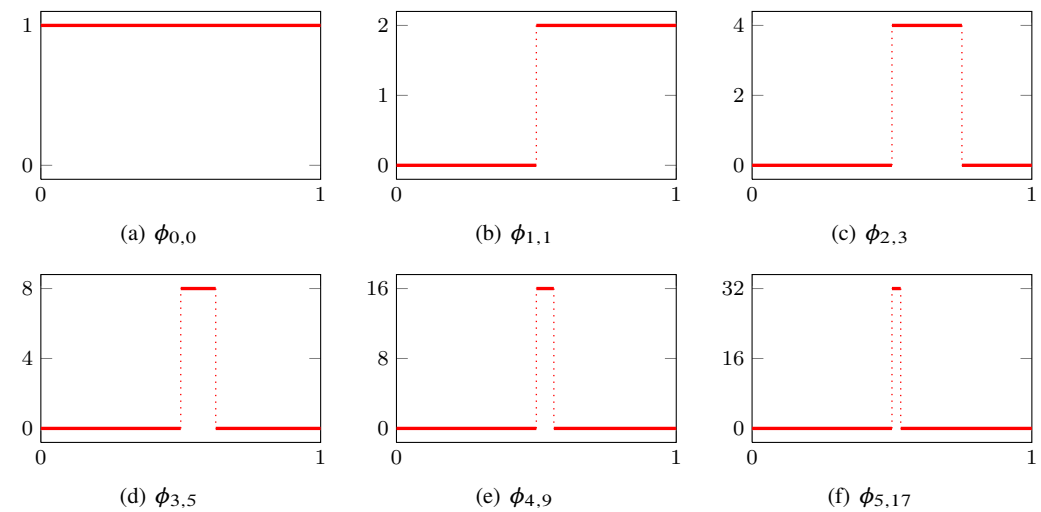

Figure 6. Examples of the first six levels of periodized Haar scaling functions

5. MODEL DEVELOPMENT

The mixed finite-element/wavelet-Galerkin model of the rotor blade undergoing unilateral contact introduced in Section 2 is based on the NASA 67 rotor, a transonic fan stage rotor containing 22 blades. The geometry [44] is commonly used for validation of aerodynamic simulation for rotating machinery codes. Limited documentation is available regarding structural analysis of the blade; Doi [15] reports the blade is manufactured from a titanium alloy with the following properties: elastic modulus of 117.2 GPa, Poisson's ratio of 0.3, density of $4539.5\,\mathrm{kg\,m^{-3}}$.

The mesh, shown in Fig. 2, is constructed in ANSYS using 20-node quadratic-hexahedral elements; the blade-foot is rigidly constrained. The mesh was adjusted until the first 30 eigenmodes converged to within 1 %. Seven nodes along the blade tip (roughly equally spaced) are selected as contact nodes (21 degrees-of-freedom). This mesh is then further synthesized through an adapted version of the Craig-Bampton method [2, 26] using 20 component modes, resulting in a final model size of 41 degrees-of-freedom. Validation of this reduced model showed mode convergence of 1 % or better for the first 20 modes, thus the mesh of the finite element model is deemed acceptable for use in the unilateral contact simulation.

The contact penalty function parameters a_c and α in Eq. (7) are selected to simulate contact with a rigid wall: $a_c = 10^4\,\mathrm{N}$, $\alpha = 5 \times 10^4\,\mathrm{cm^{-1}}$. To select these values, penalty function parameters were increased until the results converged such that small increases in the penalty function parameters negligibly affected the predicted response; further increase in the parameters did not significantly decrease wall penetration and only served to diminish the conditioning of the system. The beta-damping β in Eq. (9) is set to $\beta = 10^{-5}\,\mathrm{s}$, which results in light damping (< 0.5 %). Note, the penalty function of Eq. (7) assumes elastic contact. It is possible incorporating a restitution coefficient to simulate the dissipation found in inelastic contact could help improve convergence in the time-marching solution [22, 18].

To act as a comparison solution, the unilateral contact finite-element equations detailed above are solved using a variable-order numerical differentiation formula (NDF) time-stepping algorithm [42]. As the time-stepping solution does not solve for the periodic response directly, the solution is deemed to have converged to its periodic state when the rms of the relative error between the tip displacements for the i and $i-1$ periods is below 10^{-5} %. For boundary oscillation frequencies between $50-1000\,\mathrm{Hz}$ this generally required simulation of $100-200$ periods of vibration; this approach is possible because the structural damping causes the transient response to decay away, albeit slowly.

5.1. Weighted residual formulation

Table I lists the combination of trial and weighting functions employed in the current investigation; where wavelet families are listed (B-spline, Haar, Daubechies), it is implied the scaling functions are used according to Eq. (29). The integrals involved in Eq. (18) are computed as discrete inner products using

Table I. List of trial and weighting function combinations

Trial function	Weighting function
Fourier	Fourier
B-spline	B-spline
Daubechies 6	Daubechies 6
B-spline	Fourier
Haar	Fourier
Haar	B-spline

1024 points for all but the Galerkin formulation using Daubechies functions. For the Daubechies Galerkin cases, the inner products are derived using the connection coefficients as mentioned in Section 4.4.

6. RESULTS

The six combinations of trial and weighting functions listed in Table I are employed to solve the condensed, nonlinear weighted residual formulation given in Eq. (22) for prescribed boundary frequencies ranging between 50 Hz to 1000 Hz. The computed evolution of the blade tip displacement vs. boundary frequency for the center contact node is shown in Fig. 7, normalized over one period of vibration.

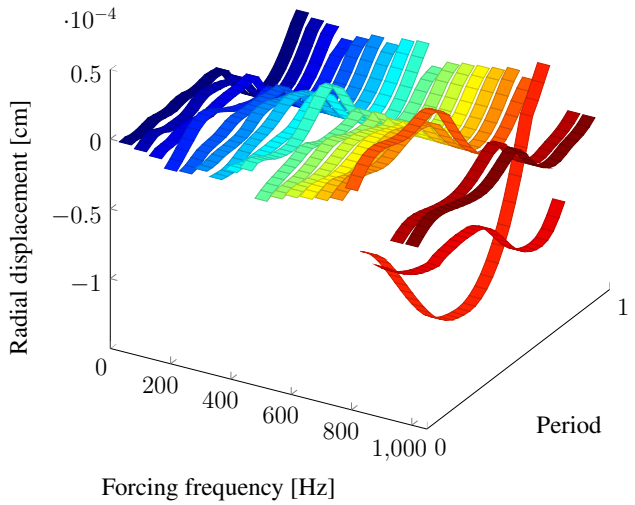

Figure 7. Evolution of the blade tip center displacement for 50 Hz to 1000 Hz boundary frequencies

Blade resonances near 320 Hz and 785 Hz are identified by the large amplitude tip deflections. Results at 450 Hz are selected to compare the basis function combinations listed in Table I; the tip displacements at this frequency are still relatively large thus large contact forces were expected. This typically results in numerical convergence difficulties thus comparison at this frequency should highlight the strengths and weakness of the proposed formulations.

6.1. Tip displacement

Samples of the predicted tip displacement responses at 450 Hz using 32 ($J = 5$) and 128 ($J = 7$) basis functions are provided in Fig. 8. All results shown are for the center contact node. All contact nodes were found to interact with casing wall and produce unique responses; the center node response was deemed a representative response thus only these results are shown for brevity.

The HBM method (Fourier:Fourier) approximates the tip displacements well using both 32 and 128 basis functions compared to the time-stepping solution. This is expected as the displacement curves are relatively smooth and well suited to the HBM method. The B-spline Galerkin formulation appears to have difficulty accurately computing the response using fewer basis functions but improves as the number of functions increases. The Daubechies Galerkin formulation (DB6:DB6) appears to perform well for both cases shown, though a quantitative analysis of the results in Sec. 6.5 show it is slightly less accurate than HBM.

The Haar:Fourier and Haar:B-spline formulations result in a stepped approximation of the tip displacement due to the blocky nature of the Haar scaling functions, particularly noticeable for lower numbers of basis functions. As the number of basis functions is increased, the step-size of the Haar function within the period is reduced, and at 128 basis functions the approximation follows the time-stepping solution closely. The benefits of using Haar scaling functions as trial functions become more evident when viewing the predicted contact forces, as discussed in Section 6.3.

6.2. Tip velocity

Consideration is also given to the accuracy with which the trial functions can predict velocities. For all displacement approximations where the trial basis functions can be differentiated pointwise to approximate velocities using Eq. (13), the following equality is used:

$$\dot{\tilde{u}}_i(t) = \sum_{k=1}^{M} a_{ik}\dot{q}_k(t). \tag{42}$$

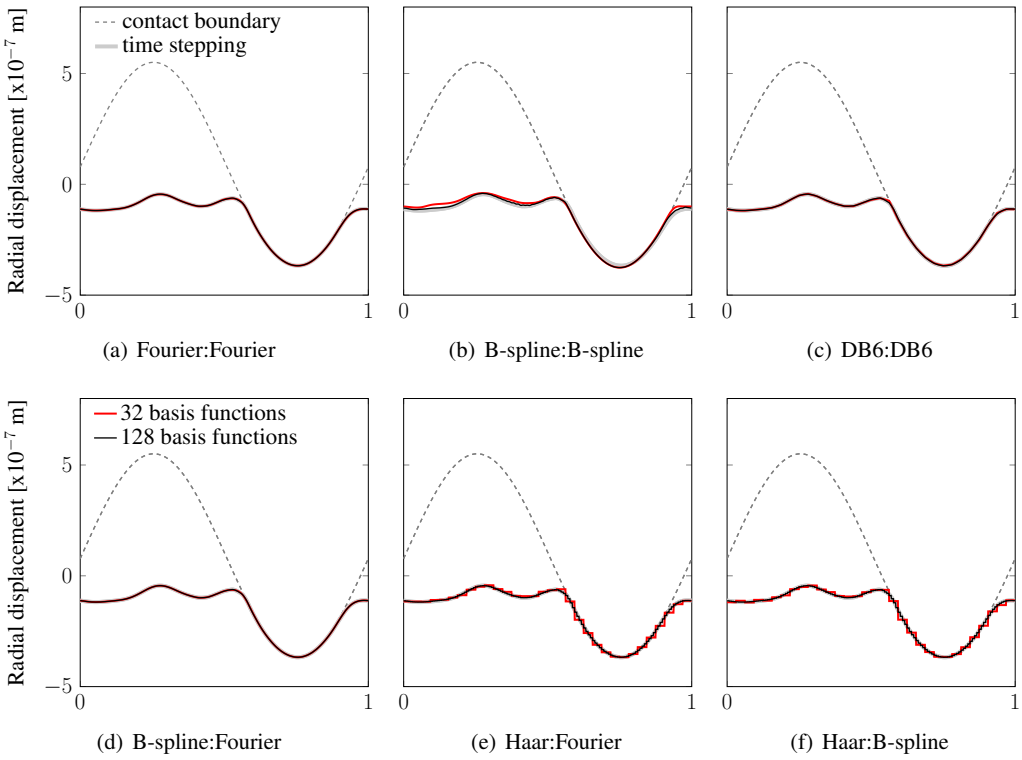

Figure 8. Blade tip center displacement over one period T at 450 Hz forcing frequency

The only cases where Eq. (42) is not valid are those involving Haar trial functions; Haar scaling functions are piecewise constant functions thus they cannot be directly differentiated in the usual sense (*i.e.* pointwise) to determine velocities. Velocities for these cases can be approximated by assuming the derivative of a Haar scaling function is the combination of a positive delta function at t_1 and a negative delta function at t_2, where t_1 corresponds to the positive jump discontinuity in the Haar scaling function and t_2 corresponds to the negative jump. Using a set of these functions as $\dot{q}_k(t)$ in Eq. (42) provides a reasonable approximation to the corresponding velocity field for cases involving Haar functions.

The approximate center-node tip velocity response at 450 Hz is plotted in Fig. 9 for all cases using both 32 and 128 basis functions. The delta function representation discussed above can be seen in Figs. 9(e) and 9(f) for the 32 basis function case; only discrete points at the tips of the delta functions are shown for the 128 basis function case for clarity of the figure.

It is visible from these approximations that there is a sharp change in velocity due to the contact condition about halfway through the period. This type of response is known to typically produce in ringing due to Gibbs phenomenon at the sharp gradient change using Fourier trial functions. While this phenomena was found to exist, it was slight and not readily visible on the plot. Interestingly, the ringing is more pronounced in the Galerkin B-spline case, suggesting this formulation may not be an optimal basis for this particular simulation.

The 128 function DB6:DB6 combination closely follows the time-stepping solution, more accurately predicting the sharp gradient changes which the HBM solution smoothed out. This is a result of a few DB6 scaling function characteristics: vanishing moments up to order 2 allowing accurate approximation of smooth curves; and the highly localized and fractal nature of the function which capture the nonsmooth changes in the response.

For cases involving Haar trial functions the functional velocity envelope is reasonably approximated by the delta function representation, especially as the number of basis functions is increased. They appear to do particularly well in capturing the rapid gradient changes.

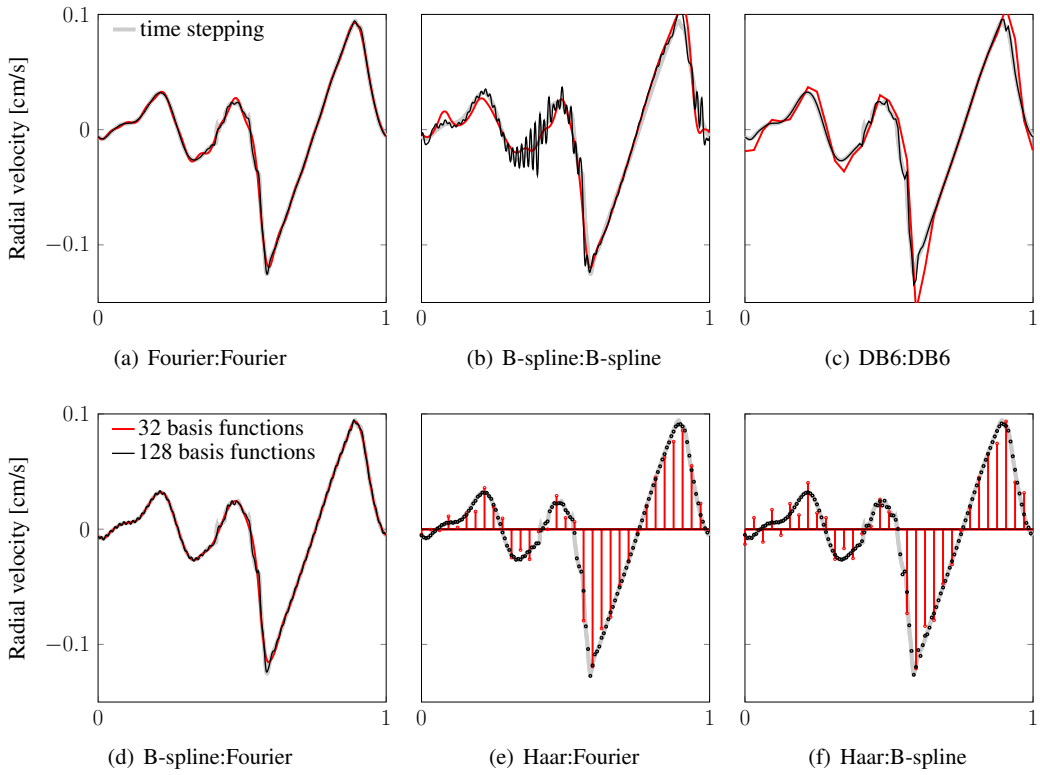

Figure 9. Blade tip center velocity over one period T at 450 Hz forcing frequency

6.3. Tip contact force

The contact forces at the blade tip, calculated using the penalty function provided in Eq. (7), are computed at the seven contact nodes simultaneously. The contact force magnitudes for the seven nodes predicted at 450 Hz using the time-stepping method are presented in Fig. 10.

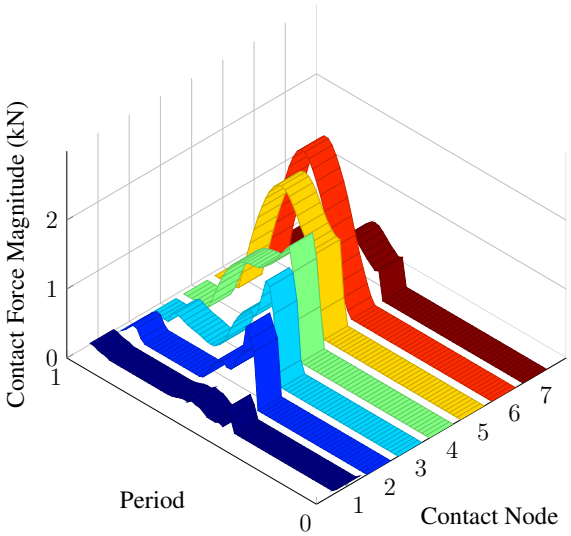

Figure 10. Contact force magnitude across all contact nodes (node 1: leading edge; node 7: trailing edge)

The contact force for the middle node predicted at 450 Hz are presented for the six combinations in Fig. 11. Notice the time duration of the contact forces coincide with the interval where the tip displacement equals the boundary displacement of Fig. 8 as this is the only period during which the blade tip is in contact with the oscillating boundary.

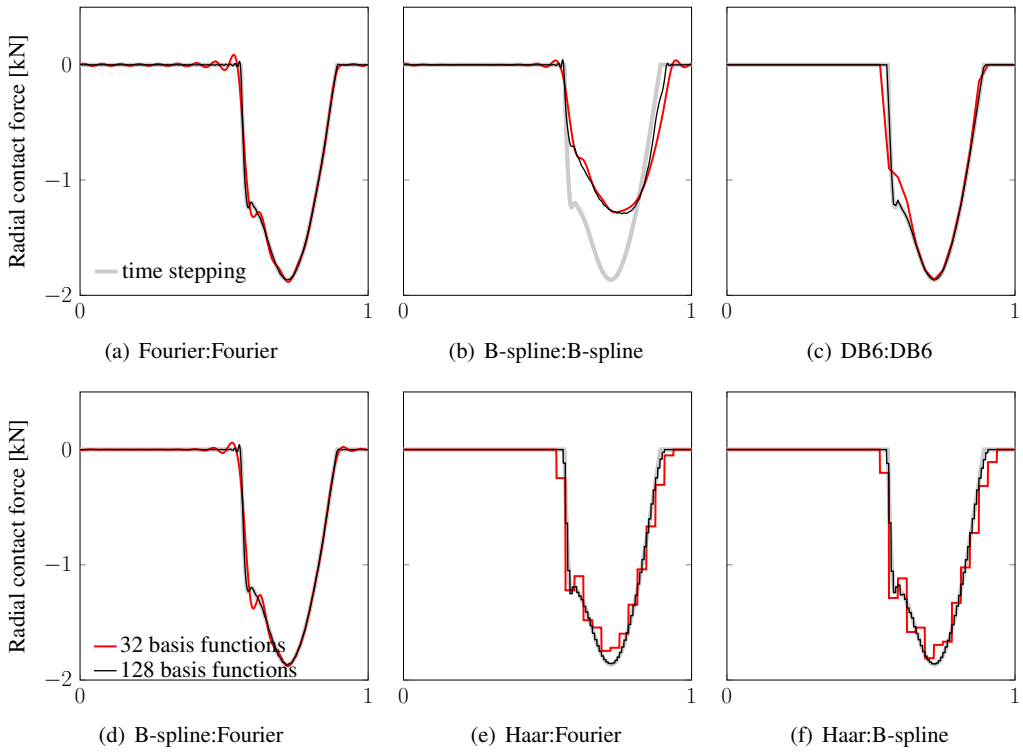

(a) Fourier:Fourier (b) B-spline:B-spline (c) DB6:DB6

(d) B-spline:Fourier (e) Haar:Fourier (f) Haar:B-spline

Figure 11. Blade tip center contact force over one period T at 450 Hz forcing frequency

The effect of Gibbs phenomenon can be seen in the HBM and Galerkin B-spline cases at the nonsmooth transition between a free and forced blade tip. When simulating contact using a rigid contact law, this ringing can be detrimental to numerical convergence as it artificially causes the blade tip to bounce repeatedly off the boundary. This can cause the nonlinear solver to diverge from the desired solution.

The DB6 Galerkin formulation does well in capturing both the smooth sections and the nonsmooth transitions, particularly using 128 basis functions. The use of Haar trial functions does especially well in locating the nonsmooth transition. It is hypothesized that if a rigid contact law is enforced the Daubechies or Haar scaling functions will perform better relative to the other functions; this will be investigated in future work.

6.4. Energy norm convergence

Convergence of the normalized energy norms for each basis combination at 450 Hz are given in Fig. 12(a). For these results the distributional form of the governing equations discussed in Section 3.3 are used in all cases. Results using the strong and weak forms of the governing equation are discussed further in Section 6.7.

The system energy is calculated as

$$E = \frac{1}{2}\dot{\tilde{\mathbf{u}}}^T \mathbf{M}\dot{\tilde{\mathbf{u}}} + \frac{1}{2}\tilde{\mathbf{u}}^T \mathbf{K}\tilde{\mathbf{u}} + E_{\text{penalty}}. \tag{43}$$

where E_{penalty} is the energy stored in the penalty springs used to enforce contact. The scalar energy norm is calculated as the rms value of the system energy E over a single period; this is then normalized by the energy norm from the time-stepping solution. The velocity terms $\dot{\tilde{\mathbf{u}}}$ are calculated as detailed in Section 6.2.

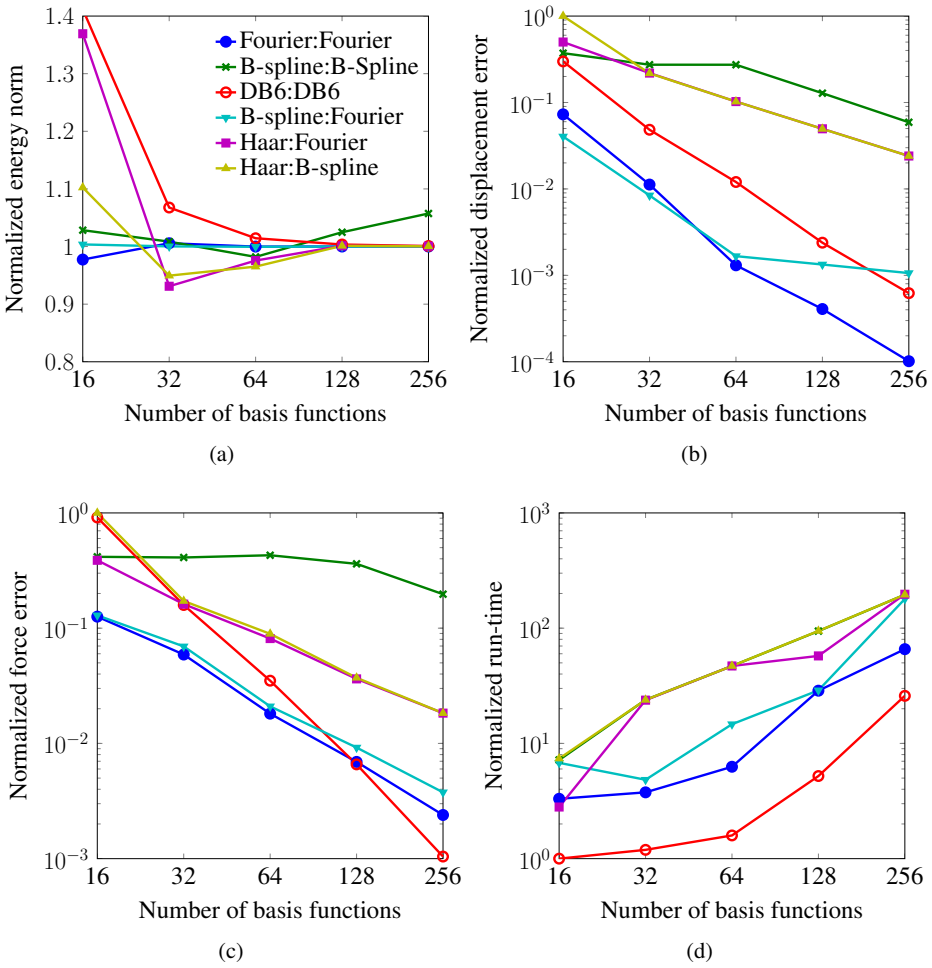

Figure 12. Convergence for center contact node at 450 Hz as the number of basis functions are increased: (a) energy norm; (b) blade tip displacement error; (c) contact force error; (d) run-time

As shown in Fig. 12(a), all combinations of trial and weighting functions converge to the time-stepping solution (*i.e.* energy norms are approximately unity using 256 basis functions). The HBM, Galerkin B-spline, and B-spline:Fourier formulations show energy norms close to unity even using relatively few basis functions. The combinations utilizing Haar trial functions tend to under-predict the system energy when few trial functions are used. This is predictable considering the blocky nature of the response (*e.g* Fig. 8(e)) which gives a coarse representation of the periodic displacement and velocity responses.

Also notice the large energy norms predicted for the DB6:DB6 formulation using 32 or few basis functions. This is due to poor representation of the response compared to the time-stepping solution. Whilst the DB6:DB6 formulation has many good attributes for solving nonsmooth contact problems, these results suggest a greater number of basis functions may be necessary to predict globally accurate solutions as compared to the HBM method (see Section 6.7 for further discussion).

6.5. Tip displacement and wall force relative error

It is also desirable to quantify the global approximation error for the blade tip displacement and resulting wall force as predicted using the weighted residual combinations. The time-stepping solution is again used as a comparison solution and the results for the center contact node are shown. The rms displacement error over one period is plotted for the six basis function combinations in Fig. 12(b), while the rms wall force error is plotted in Fig. 12(c).

As shown in Fig. 12(b), the HBM and B-spline:Fourier approaches have the lowest error when 128 or few basis functions are used. This quantifies the visual evidence reported in Section 6.1. The relative error using Haar trial functions is largest out of the combinations investigated. This is expected due to the blocky nature of the Haar scaling functions; however the mid-points of the Haar functions match very well to the trend of the time-stepping solution. This suggests that if only a low resolution approximation of the response is required, the Haar scaling functions still perform well.

The Galerkin DB6 case performs reasonably well throughout, though is always outperformed by the Fourier cases. This is attributed to the fact the displacement curves are relatively smooth thus well suited to HBM. The benefits of the nonsmooth DB6 scaling functions to accurately predict sharp gradient changes is not beneficial here. However, as shown in the force error plot Fig. 12(c), the Daubechies wavelets show promise in predicting the non-smooth contact force.

The relative errors in the predicted contact forces are presented in Fig. 12(c). The HBM and B-spline:Fourier formulations perform the best when fewer basis functions are employed, but the DB6:DB6 case produce the most accurate prediction of the contact force once 256 functions are employed. This is again attributed to the ability of the Daubechies basis to represent sharp gradient changes, such as the transition from free vibration to contact with the casing. The Haar:Fourier formulation does not perform as well, but not as poorly as expected. This is attributed to the Haar functions ability to accurately capture the flat portion of the force response, and adequately represent the zone of contact.

6.6. Relative computational cost

While each formulation requires computation of the same number of unknowns for a given basis size, the computational cost of each method was found to differ. The difference between the methods shown in Fig. 12(d) is mainly due to the number of iterations required for the non-linear solver to converge. The Galerkin B-spline and methods involving Haar functions were found to require significantly more iterations in general compared to the other methods.

The DB6 Galerkin formulation required the least amount of computing time for the non-linear solution to converge at all basis sizes. In general, this formulation required significantly fewer iterations for the non-linear solver to reach the convergence criteria. It is hypothesized that this is due to the more accurate representation of the contact forces which prevented numerical “bouncing” or “ringing”.

The HBM solution also performed very well. Note, fast-Fourier transforms were not employed in this investigation to allow a more balanced comparison between the methods. If the FFT method were incorporated into the code this would significantly reduce run times for HBM cases. Fast-wavelet transforms are also available for Daubechies wavelets and will be investigated further to determine the benefits to computational time.

6.7. Principal Angles Between Subspaces

The solution predicted using a weighted residual technique must exist in the approximate solution space defined by the trial and weighting functions chosen. The Galerkin and Petrov-Galerkin approaches require the projection of the trial function basis (and/or its derivative) onto the weighting function basis (and/or its derivative); it is within this projected space that the approximate solution is determined. Increasing the dimensionality of either the trial or weighting functional bases only improves the prediction accuracy if the inner product of the bases expands the approximate solution space to encapsulate more of the $L^2(\mathbb{S}^1)$ space.

Principal angles provide a measure of the commonality or “overlap” of the trial and weighting function spaces, where Shonkwiler [23] shows that there are an equal number of principal angles as trial (or weighting) functions. If the trial and weighting functions span the same space, all the principal angles will equal zero and the approximate solution space will be large. If the trial and weighting functions are orthogonal to each other, all the principal angles will equal 90° and the approximate solution space will be null. The more principal angles with values close to 0 implies the projection of the trial functions onto the weighting functions span a larger approximate solution space and thus can potentially provide more accurate predictions.

The principal angles for the six Galerkin and Petrov-Galerkin combinations with 64 degrees-of-freedom are provided in Fig. 13 for the three projections required in the weaker form (distributional approach)

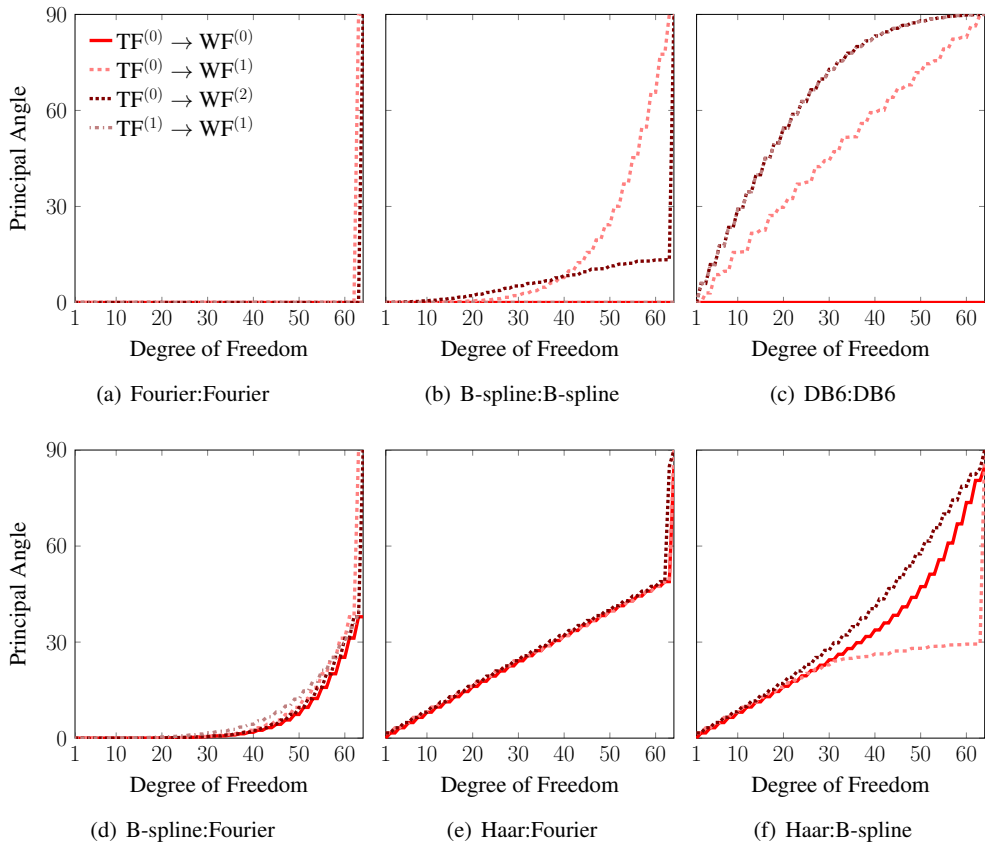

Figure 13. Principal angles for Galerkin and Petrov-Galerkin subspaces with 64 basis functions. TF signifies trial function, WF signifies the weighting function, and the superscript (n) signifies the derivative order.

outlined in Section 3.3: $TF^{(0)} \rightarrow WF^{(0)}$; $TF^{(0)} \rightarrow WF^{(1)}$; $TF^{(0)} \rightarrow WF^{(2)}$. For example, $TF^{(0)} \rightarrow WF^{(1)}$ signifies the trial function basis being projected onto the first derivative of the weighting function basis. Also included are the principal angles for $TF^{(1)} \rightarrow WF^{(1)}$ which is required if the weak form is used.

As expected the Fourier:Fourier combination has principal angles equal to zero for all but a couple of dimensions. Consider $TF^{(0)} \rightarrow WF^{(2)}$ for example: the trial function basis contains the 0^{th} Fourier term (*i.e.* the constant offset vector), whereas in the second derivative of the weighting functions this vector is null. Thus when $TF^{(0)}$ is projected onto $WF^{(2)}$ the information contained in the 0^{th} Fourier term is lost, hence the single 90° principal angle value. All other basis vectors are shared by both spaces so the remaining 63 principal angles are nil as illustrated in Fig. 13(a).

This property is not shared for all Galerkin bases. In Fig. 13(b) the principal angles for the B-Spline Galerkin method are shown and have a greater range than the Fourier:Fourier case. This implies the projected solution space is somewhat smaller for the B-Spline Galerkin approach. This aides in the explaining why the relative errors shown in Fig. 12(b) and 12(c) are larger for B-Spline:B-Spline than for Fourier:Fourier.

Note that for all the Galerkin combinations $TF^{(0)} \rightarrow WF^{(0)}$ and $TF^{(1)} \rightarrow WF^{(1)}$ the principal angles are all zero. This is because for these cases the trial and weighting function bases are the same. This implies the well-known fact that the weak formulation may provide better prediction accuracy than the distributional formulation, where $TF^{(0)} \rightarrow WF^{(2)}$ is required. Numerical simulation verifies this hypothesis, but the improvement in accuracy is orders of magnitude less than the relative error thus results for the weak form are not included in the discussion.

For the Petrov-Galerkin cases shown in Fig. 13(d) to 13(f), all the required projections result in a reduction of the solution space. The combinations involving Haar functions as the trial basis tend to have

large mean principal angles, which attests to the Haar:Fourier and Haar:B-Spline combinations performing poorly according to Fig. 12(b) and 12(c).

Fig. 13(c) shows the DB6:DB6 formulation also has a large mean for its principal angles. This aids in explaining why the numerical convergence of this formulation was poor using 64 basis functions or fewer; the approximate solution space is relatively small. As the total number of trial and weighting functions is increased, this increases the number of degrees-of-freedom with low principal angle values making possible an accurately predicted solution.

7. FURTHER BLADE RESULTS

While this investigation focuses on determining effective functional basis for predicting blade response under unilateral contact conditions, a few post-processed FEA results are included below to highlight the practicality of the proposed approach.

7.1. Full-field result profiles

Once the periodic displacements from the reduced FEA model are computed using the wavelet-Galerkin method, the full-field displacements of the blade can be reproduced using the adapted Craig-Bampton method [2, 26]; Fig. 14 shows the displacement field during the periodic response at 320 Hz. From these results, stress and strain contours can be created using standard finite element methods.

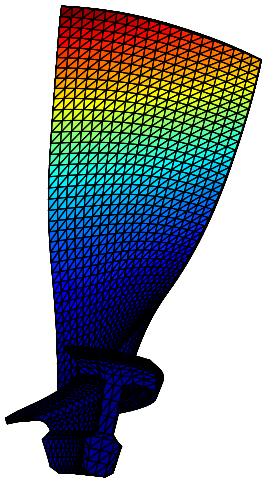

Figure 14. Displacement field in deformed blade during a single time-step of periodic response at 320 Hz

7.2. Forced response

Another result of interest is the ability to construct the frequency response function for the unilateral contact condition. The penalty function simulating contact is effectively a stiffening condition, thus the resonant peaks for the system are expected to increase in frequency relative to the no-contact response.

To capture this nonlinear response an arc-length continuation method [19] is utilized. The frequency response function over one of the system's resonant frequencies is shown in Fig. 15 using both the HBM and Galerkin DB6 combinations with 256 basis functions. To compute the forced response, the position of the rigid boundary is kept constant and a harmonic point load is introduced to the contact node.

As shown, the stiffening behaviour of the unilateral contact condition is captured by both trial:weighting function combinations; other combinations showed similar approximations. These results are promising as it implies the arc-length continuation method can be accurately applied to both Galerkin and Petrov-Galerkin approaches using the distributional formulation for a number of different bases.

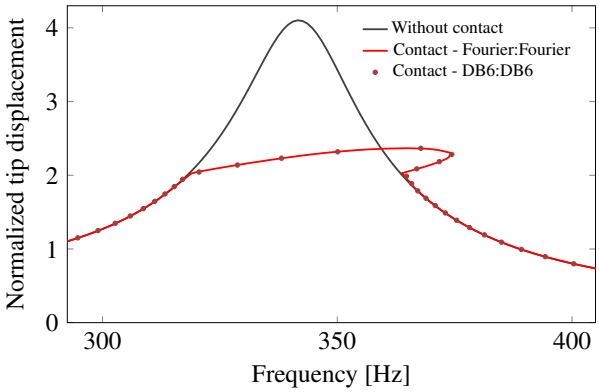

Figure 15. Frequency response function over the 1st fundamental frequency of the unilateral contact system

8. CONCLUSIONS

The method of weighted residuals for capturing the periodic responses of unilateral contact problems has been investigated on an industrial blade for a number of trial:weighting function combinations. The contact condition is simulated using an exponential penalty function approach. To extend the allowable trial function bases, a weak and a distributional formulations are presented which transfer trial function continuity requirements to the weighting functions. This allowed piecewise constant Haar scaling functions to be used as a trial basis in the current investigation. Results show that a number of trial:weighting function combinations produce accurate solutions which rapidly converge as the size of the discrete spaces is increased. As expected, Fourier functions perform well as a trial basis, though nonsmooth functions such as Haar and Daubechies scaling functions are also attractive since they provide comparable prediction accuracy and even out perform the Fourier functions in some measures.

Research is continuing on this subject. The goal is to improve on the penalty approach by implementing an exact unilateral contact Lagrange multiplier method. The hypothesis is that nonsmooth trial functions will be able to approximate these flat sections better than Fourier functions, and thus could provide better contact force estimation and improved convergence for nonlinear solution algorithms.

Furthermore, the results from this investigation show that the prediction accuracy using wavelet scaling functions may increase at a greater rate than Fourier function when the global scale is increased. However, this global scale increase may not be optimal. In most cases the coarse wavelet functions can reasonably predict general trends in the response, it is only locations of sharp gradient changes where fine scale functions are required (*i.e.* very short compact support); this local increase in resolution is not possible with Fourier trial functions [29]. Future work will focus on resolving only these high gradient areas using wavelets and leaving coarse scaling functions to describe the smooth sections. Increased accuracy shall be met while minimizing the number of basis functions required.

9. ACKNOWLEDGEMENTS

The authors would like to thank Professor Gantumur Tsogtgerel from McGill University and Professor Stéphane Junca from University of Nice Sophia-Antipolis for their insightful discussions regarding wavelets and functional analysis. Thanks also go to Alain Batailly and Markus Meingast for support concerning the Craig-Bampton reduction of the blade. Jones would also like to acknowledge the Tomlinson Postdoctoral Fellowship for partially funding this research.

A. SOBOLEV SPACES

In the paper, $\mathbb{S}^1$ denotes the circle compact support that can be identified to the interval $(0, 1)$ on the real line. Due to the periodicity conditions in time that should be satisfied by the solution, integral forms are readily derived on this set.

Below is a list of the Sobolev spaces defined on $\mathbb{S}^1$ with brief descriptions on how they relate to the current investigation:

- $L^2(\mathbb{S}^1)$ is the space of square integrable functions on the circle.
- $H^1(\mathbb{S}^1)$ is the space of square integrable functions on the circle in which the first derivative (in a distributional sense) is also square integrable.
- $H^2(\mathbb{S}^1)$ is the space of square integrable functions on the circle in which the first and second derivatives (in a distributional sense) are also square integrable.
- $L^2(\mathbb{S}^1)^N$ is the space containing N square integrable functions on the circle, where N is the number of spatial degrees-of-freedom in the current investigation—this is analogous for $H^1(\mathbb{S}^1)^N$ and $H^2(\mathbb{S}^1)^N$.

REFERENCES

[1] Acary, Vincent and Bernard Brogliato. *Numerical methods for nonsmooth dynamical systems*. Springer, 2008. [ISBN: 9783540753919].

[2] Batailly, Alain, Mathias Legrand, Antoine Millecamps, and François Garcin. "Numerical-experimental comparison in the simulation of rotor/stator interaction through blade-tip/abradable coating contact". *Journal of Engineering for Gas Turbines and Power*, 134(8) 2012. [hal-00746632].

[3] Bathe, Klaus-Jürgen. *Finite element procedures in engineering analysis*. Prentice-Hall, 1982. [ISBN: 9780133173055].

[4] Berberian, Sterling. *Introduction to Hilbert space*. American Mathematical Society, 1999. [ISBN: 9780821819128].

[5] Beylkin, Gregory. "On the representation of operators in bases of compactly supported wavelets". *SIAM Journal of Numerical Analysis*, 6(6):1716–1740, 1992. [hal-01322928].

[6] Beylkin, Gregory and James Keiser. "On the adaptive numerical solution of nonlinear partial differential equations in wavelet bases". *Journal of Computational Physics*, 132(2):233–259, 1997. [hal-01322927].

[7] Blatter, Christian. *Wavelets a primer*. A K Peters CRC Press, 1998. [ISBN: 9781568811956].

[8] Burgos, Rodrigo, Raul e Silva, and Marco Santos. "Direct solution of differential equations using the wavelet-Galerkin method". *Mecanica Computacional*, XXIX:4573–4584, 2010. [hal-01333839].

[9] Burrus, Sydney, Ramesh Gopinath, and Haitao Guo. *Introduction to wavelets and wavelet transforms: a primer*. Prentice Hall, 1998. [ISBN: 9780134896007].

[10] Cameron, Timothy and Jerry Griffin. "An alternating frequency/time domain method for calculating the steady-state response of nonlinear dynamic systems". *Journal of Applied Mechanics, Transactions ASME*, 56(1):149–154, 1989. [hal-01333697].

[11] Chen, Ming-Quayer, Chyi Hwang, and Yen-Ping Shih. "The computation of wavelet-Galerkin approximation on a bounded interval". *International Journal for Numerical Methods in Engineering*, 39(17):2921–2944, 1996. [hal-01330583].

[12] Christon, Mark and David Roach. "The numerical performance of wavelets for PDEs: the multi-scale finite element". *Computational Mechanics*, 25(2-3):230–244, 2000. [hal-01333698].

[13] Cook, Robert, David Malkus, Michael Plesha, and Robert Witt. *Concepts and Applications of Finite Element Analysis*. 4th edition. John Wiley & Sons, 2001. [ISBN: 9780471356059].

[14] Daubechies, Ingrid. *Ten lectures on wavelets*. CBMS-NSF Regional Conference Series in Applied Mathematics. Society for Industrial and Applied Mathematics, 1992. [ISBN: 0898712742]. [10.1137/1.9781611970104].

[15] Doi, Hirofumi. "Fluid/structure coupled aeroelastic computations for transonic flows in turbomachinery". PhD thesis. Stanford University, 2002. [tel-01333735].

[16] Durran, Dale. *Numerical Methods for Fluid Dynamics. With Applications to Geophysics*. 2nd edition. Volume 32. Texts in Applied Mathematics. Springer, 2010. [ISBN: 9781441964113].

[17] Erlebacher, Gordon, Yousuff Hussanini, and Leland Jameson. *Wavelets: Theory and applications*. Oxford University Press, 1996. [ISBN: 0195094239].

[18] Flores, Paulo, Margarida Machado, Miguel Silva, and Jorge Martins. "On the continuous contact force models for soft materials in multibody dynamics". *Multibody System Dynamics*, 25(3):357–375, 2011. [hal-01333699].

[19] Groll, Gotz von and David Ewins. "The harmonic balance method with arc-length continuation in rotor/stator contact problems". *International Journal for Numerical Methods in Engineering*, 241(2):223–233, 2001. [hal-01333704].

[20] Haar, Alfréd. "Zur Theorie der orthogonalen Funktionensysteme Erste Mitteilung". *Mathematishe Annalen*, 69(3):331–371, 1910. [hal-01333722].

[21] Holschneider, Matthias. "Wavelet analysis on the circle". *Journal of Mathematical Physics*, 31(1):39–44, 1990. [hal-01333726].

[22] Hunt, Kenneth and Erskine Crossley. "Coefficient of restitution interpreted as damping in vibroimpact". *Journal of Applied Mechanics*, 42(2):440–445, 1975. [hal-01333795].

[23] Jiang, Sheng. "Angles between Euclidean subspaces". *Geometriae Dedicata*, 63(2):113–121, 1996. [hal-01333799].

[24] Lapidus, Leon and John Seinfeld. *Numerical solution of ordinary differential equations*. Academic Press, 1971. [ISBN: 0124366503].

[25] Laxalde, Denis and Mathias Legrand. "Nonlinear modal analysis of mechanical systems with frictionless contact interfaces". *Computational Mechanics*, 47(4):469–478, 2011. [hal-00492775].

[26] Legrand, Mathias, Alain Batailly, Benoit Magnain, Patrice Cartraud, and Christophe Pierre. “Full three-dimensional investigation of structural contact interactions in turbomachines”. *Journal of Sound and Vibration*, 331(11):2578–2601, 2012. [hal-00660863v3].

[27] Legrand, Mathias, Sébastien Roques, Christophe Pierre, Patrice Cartraud, and Bernard Peseux. “n-dimensional Harmonic Balance Method extended to non-explicit nonlinearities”. *Revue Européenne de Mécanique Numérique*, 15(1-2-3):269–280, 2006. [hal-00354486].

[28] Leine, Remco and Henk Nijmeijer. *Dynamics and bifurcations of non-smooth mechanical systems*. 2nd edition. Volume 18. Lecture Notes in Applied and Computational Mechanics. Springer, 2006. [ISBN: 9783540219873].

[29] Li, Xin, Bo Hu, Xie-Ting Ling, and Xuan Zeng. “A wavelet balance approach for steady-state analysis of nonlinear circuits”. *The 2001 IEEE International Symposium on Circuits and Systems*. Volume 3. 2. 2001: 73–76. [hal-01333733].

[30] Liu, Gui Rong and Siu Sin Quek. *Finite element method: a practical course*. Butterworth-Heinemann, 2013. [ISBN: 9780080983561].

[31] Mallat, Stéphane. *A wavelet tour of signal processing. The Sparse Way*. 3rd edition. Elsevier/Academic Press, 2009. [ISBN: 0123743702].

[32] Meyer, Yves. *Ondelettes. Ondelettes et opérateurs*. Volume 1. Hermann, 1990. [ISBN: 2705661255].

[33] Mickens, Ronald. “Comments on the method of harmonic balance”. *Journal of Sound and Vibration*, 94(3):456–460, 1984. [hal-01333728].

[34] Nielsen, Ole Møller. “Wavelets in Scientific Computing”. PhD thesis. Technical University of Denmark, 1998. [tel-00803835].

[35] Padova, Corso, Jeffery Barton, Michael Dunn, and Steve Manwaring. “Experimental results from controlled blade tip/shroud rubs at engine speed”. *Journal of Turbomachinery*, 129:713–723, 2007. [hal-01333702].

[36] Park, Myounggu, Young-Ha Hwang, Yun-Seung Choi, and Tae-Gu Kim. “Analysis of a J69-T-25 engine turbine blade fracture”. *Engineering Failure Analysis*, 9:593–601, 2002. [hal-01333729].

[37] Pernot, Stéphane and Claude-Henri Lamarque. “A wavelet-Galerkin procedure to investigate time-periodic systems: transient vibration and stability analysis”. *Journal of Sound and Vibration*, 245(5):845–875, 2001. [hal-00814563v1].

[38] Pilipchuk, Valery. “Application of special nonsmooth temporal transformations to linear and nonlinear systems under discontinuous and impulsive excitation”. *Nonlinear Dynamics*, 18(3):203–234, 1999. [hal-01333694].

[39] Reddien, George. “Projection methods for two-point boundary value problems”. *SIAM Review*, 22(2):156–171, 1980. [hal-01333730].

[40] Restrepo, Juan Mario and Gary Leaf. “Inner product computations using periodized Daubechies wavelets”. *International Journal for Numerical Methods in Engineering*, 40(19):3557–3578, 1997. [hal-01323007].

[41] Schindler, Thorsten and Vincent Acary. “Timestepping schemes for nonsmooth dynamics based on discontinuous Galerkin methods: Definition and outlook”. *Mathematics and Computers in Simulation*, 95:180–199, 2014. [inria-00595460].

[42] Shampine, Lawrence and Mark Reichelt. “The Matlab ODE Suite”. *SIAM Journal on Scientific Computing*, 18:1–22, 1997. [hal-01333731].

[43] Strang, Gilbert and Truong Nguyen. *Wavelets and filter banks*. Wellesley-Cambridge Press, 1996. [ISBN: 0961408871].

[44] Strazisar, Anthony, Jerry Wood, Michael Hathaway, and Kenneth Suder. “Laser anemometer measurements in a transoic axial-flow fan rotor”. *NASA STI/Recon Technical Report N*, 90:11245, 1989. [hal-01337330].

[45] Studer, Christian. *Numerics of unilateral contacts and friction. Modeling and numerical time integration in non-smooth dynamics*. Volume 47. Lecture Notes in Applied and Computational Mechanics. Springer, 2009. [ISBN: 3642010997]. [10.1007/978-3-642-01100-9].

[46] Wang, Jhy-Horng and W. K. Chen. “Investigation of the vibration of a blade with friction damper by HBM”. *Journal of Engineering for Gas Turbines and Power*, 115(2):294–299, 1993. [hal-01333736].

[47] Wang, Yu. “Dynamics of unsymmetric piecewise-linear/non-linear systems using finite elements in time”. *Journal of Sound and Vibration*, 185(1):155–170, 1995. [hal-01333696].

[48] Williams, John and Kevin Amaratunga. “Introduction to wavelets in engineering”. *International Journal for Numerical Methods in Engineering*, 37(14):2365–2388, 1994. [hal-01311772].

[49] Wriggers, Peter. *Computational Contact Mechanics*. Springer, 2006. [ISBN: 9783540326083].